Controlling flow separation on a thick airfoil using backward traveling waves

A. M. Akbarzadeh* and I. Borazjani.†
J. Mike Walker ’66 Department of Mechanical Engineering, Texas A&M University, College Station, TX 77843, USA

Large eddy simulations (LES) of low Reynolds number flow (Re=50,000) over a NACA0018 airfoil are performed to investigate flow control at the stall angle of attack (15 degrees) by low-amplitude surface waves (actuations) of different type (backward/forward traveling and standing waves) on the airfoil’s suction side. It is found that the backward (toward downstream) traveling waves, inspired from aquatic swimmers, are more effective than forward traveling and standing wave actuations. The results of simulations show that a backward traveling wave with a reduced frequency $f^* = 4$ ($f^* = fL/U$, f: frequency, L: chord length, U: free flow velocity) a nondimensional wavelength $\lambda^* = 0.2$ ($\lambda^* = \lambda/L$, λ: dimensional wavelength), and a nondimensional amplitude $a^* = 0.002$ ($a^* = a/L$, a : dimensional amplitude) can suppress stall. In contrast, the flow over the airfoil with either standing or forward traveling wave actuations separates from the leading edge similar to the baseline. Consequently, the backward traveling wave creates the highest lift to drag ratio. For traveling waves at a higher amplitude (a^*=0.008), however, the shear layer becomes unstable from the actuation point and creates periodic coherent structures. Therefore, the lift coefficient decreases compared to the low amplitude case.

Nomenclature

L = airfoil chord length

$s = 0.1L$ = airfoil spanwise length

U = free flow velocity

ρ = density of the fluid

---

[*] PhD student, J. Mike Walker ’66 Department of Mechanical Engineering, Texas A&M University, College Station, TX 77843, USA

[†] Associate Professor, J. Mike Walker ’66 Department of Mechanical Engineering, Texas A&M University, College Station, TX 77843, USA

ν = kinematic viscosity

p = pressure

a = maximum amplitude of oscillation

AOA = angle of attack

λ = wavelength

$\lambda^* = \lambda / L$ = nondimensional wave length

f = frequency

$f^* = fL/U$ = reduced frequency

$C = f\lambda$ = wave speed

$C^* = C/U$ = nondimensional wave speed

$\overline{F_D}$ = mean drag force per unit of the span of the airfoil

$\overline{F_L}$ = mean lift force per unit of the span of the airfoil

$\overline{C_D} = \frac{\overline{F_D}}{0.5\rho U^2 L}$ = mean drag coefficient

$\overline{C_L} = \frac{\overline{F_L}}{0.5\rho U^2 L}$ = mean lift coefficient

$\overline{C_{po}}$ = power coefficient

$Re = LU/\nu$ = Reynolds number

u_τ = friction velocity

I. Introduction

Low Reynolds number ($Re < 500,000$) aerodynamics is an active research area as it has applications in micro-air vehicles (MAVs) and small unmanned aerial vehicles (UAVs) [1, 2]. At a low Reynolds number, the momentum of the laminar boundary layer on the upper surface of the airfoil (suction side) decreases due to viscous forces [3]. The decrease of flow momentum near the surface of an airfoil results in boundary layer separation, which generates performance losses, i.e., an increase in the drag and a decrease in the lift. By increasing the angle of attack (AOA) beyond the stall angle, lift coefficient decreases and drag increases significantly. Various active flow control techniques such as steady blowing [4–6], periodic suction and blowing [7–12], and surface morphing [13–17] have been applied to delay stall. These flow control techniques have been studied experimentally [12, 13, 18, 19] and numerically using

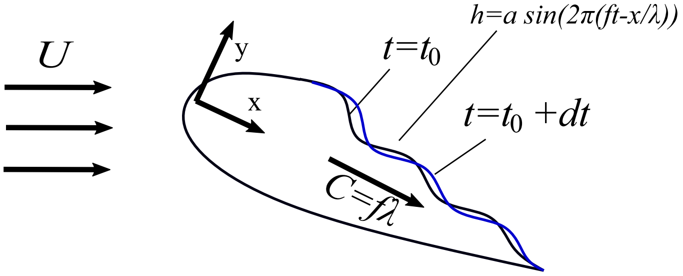

Fig. 1 The schematic of backward wave traveling wave surface morphing. The backward traveling wave propagates from the leading edge toward the trailing edge.

different turbulence modeling approaches such as direct numerical simulation (DNS) [20, 21], large eddy simulation (LES) [22–24], and Reynolds-Averaged-Navier-Stokes (RANS) [23].

The concept of changing the shape of an airfoil using flaps and slats, or vibrating its surface is called morphing. The morphing can be employed in several forms, including trailing edge flaps (TEF) [15, 17, 25, 26], leading edge flaps (LEF) [14, 16, 27], and suction side vibrations [13, 20, 21, 28, 29]. The leading edge and trailing edge flaps conventionally work based on adapting the shape of an airfoil by changing either the radius of the leading edge, or the camber of the trailing edge [30]. Typically, changing the shape of an airfoil requires large deformations which can be done by servomotors. In contrast to TEF and LEF, morphing by surface vibrations, which is referred to as surface morphing hereafter, can be performed using light, low-power piezoelectric actuators [18, 19].

Flow control via surface morphing has been investigated in several studies [20, 21, 28, 29]. Munday et al. [28, 31] reported up to 60% decrease in flow separation. Recently, Jones et al. [13] reported a delay in the onset of stall by morphing the suction side of a NACA4415 airfoil in which the fibers of piezoelectric materials covered about 80% of the whole suction side. In these studies, the oscillations of the surface were in the form of a standing wave [13] or a simple vibration [28], which accelerates the fluid adjacent to the surface along its normal direction. These types of surface morphing reduce flow separation by triggering the boundary layer instability and increasing the mixing of high momentum fluid of the separated shear layer to the low momentum fluid of the reverse flow zone [8, 13], similar to other periodic excitation methods. Nevertheless, the morphing can increase the boundary layer momentum directly if the surface vibrations be in the form of backward (opposite direction to the forward motion of an airfoil, i.e., toward downstream) traveling waves (Fig. 1) because traveling waves can increase the fluid momentum along their propagation direction [32, 33], e.g., backward traveling waves, in which the wave is propagated from the leading edge toward the trailing edge, can increase the streamwise momentum. Previous studies [33–35] has shown that backward traveling wave deformations can reduce flow separation. Recently, Akbarzadeh and Borazjani [35] observed that low amplitude ($a = 0.01L$) high frequency ($f^* = fL/U = O(20)$) backward traveling waves can reduce flow separation over an inclined plate.

Using traveling waves to control flow separation is inspired from aquatic swimmers as they propel themselves by undulations in the form of backward traveling waves [36, 37]. It has been observed that traveling waves can reduce flow separation in different flow regimes and applications, including the turbulent boundary layer of a turbulent channel [32, 33] and bluff bodies such as a circular cylinder [34] and an inclined plate [35]. Recently, Akbarzadeh and Borazjani [38] performed large eddy simulations (LES) of flow over a NACA0018 airfoil at prestall angle of attack of 10^o to investigate the role of traveling oscillations on the suction side. They observed that the lift coefficient might increase up to 4% by backward traveling wave oscillations. However, flow control is more effective at higher angles of attack, i.e., near the stall angle [7]. Inspired from the impact of traveling waves on reducing flow separation over bluff bodies and recent developments in smart materials [18, 39, 40], which have facilitated the generation of such low-amplitude traveling waves [41], our previous work is extended to investigate the impact of oscillations on the suction side with different waveforms, including backward/forward traveling and standing waves for NACA0018 at the stall angle of attack ($AOA = 15^o$).

Previous studies on surface morphing with standing waves [13, 21, 29] have shown that the amplitude and frequency of the oscillations are the main parameters affecting flow separation. However, when the oscillations are in the form of traveling waves, wavelength and wave speed (product of wavelength and frequency) can also influence the flow separation [35, 36]. For example, it is found that increasing the wave speed by increasing the frequency decreases the flow separation [32, 33, 36], but increasing the wave speed by increasing the wavelength does not necessarily decrease the flow separation [35]. Here, the effect of amplitude, frequency, and wave speed of traveling waves at a constant wavelength ($\lambda = 0.2L; L$: chord length) is studied.

The rest of this manuscript is organized as follows. In §II the governing equations and numerical method for solving the turbulent flow is illustrated. The results, including time-averaged and instantaneous ones are presented in §III. Finally, the concluding remarks are expressed in section IV.

II. Methods

Numerical simulations are performed for a thick airfoil (NACA0018) and the angle of attack is chosen to be 15^o as it has been observed that NACA0018 stalls near 15^o [23, 42, 43]. The simulation set-up and the numerical method for solving the problem is the same as our previous publication [38], in which the airfoil was at a prestall condition ($AOA = 10^o$). The free stream velocity (U) and the airfoil chord length (L) are, respectively, the characteristic velocity and length. The simulation set-up, including the fluid mesh and the airfoil geometry, is presented in Fig. 2. The flow is in a Cartesian frame (Fig. 2), in which x, y and z are along streamwise, vertical and spanwise directions, respectively. The suction side of the airfoil undergoes an actuation which can be either a traveling or standing wave deformation, as it is shown in Fig. 2b. To calculate the new position of the suction side of the airfoil under motion in the original Cartesian frame (x, y, z), a local frame (X, Y, Z) is defined, i.e., its origin is at the leading edge and is rotated by the angle of attack (Fig. 2b). The backward traveling wave oscillation ($h(X, t)$) prescribed along Y direction, is:

$$h^*(X, t) = a^*(X) \sin(2\pi(f^* t^* - X^*/\lambda^*)), \tag{1}$$

where $h^* = h/L$ is the nondimensional displacement of the suction-side, $f^* = fL/U$ is the reduced frequency, $\lambda^* = \lambda/L$ is the nondimensional wavelength, and $t^* = tU/L$ is the nondimensional time, $X^* = X/L$ is the nondimensional streamwise length that starts from the leading edge, and $a^*(X) = a(X^*)/L$ is the amplitude of the wave which starts from $X = 0.1L$ to $X = 0.85L$. The amplitude is constant and equal to its maximum value $a^* = a/L$ from $X = 0.2L$ to $X = 0.8L$ and decreases linearly toward leading and trailing edges. Here, the parameters with (*) symbol are nondimensional. The schematic of a backward traveling wave, in which the wave propagates with wave speed C^* from the leading edge toward the trailing edge is depicted in Fig. 1. To investigate the effect of actuation type, a standing and a forward traveling wave actuation have also been employed on the suction side. The corresponding equation for a forward traveling wave, in which the wave propagates towards upstream, is:

$$h^*(X, t) = a^*(X) \sin(2\pi(f^* t^* + X^*/\lambda^*)), \tag{2}$$

and the standing wave oscillation has the following deformation:

$$h^*(X,t) = a^*(X)\sin(2\pi f^* t^*)\sin(2\pi X^*/\lambda^*), \tag{3}$$

where the parameters of Eqns.2 and 3 are same as Eqn. 1.

Equations governing the flow are unsteady, three-dimensional, incompressible, filtered Navier-Stokes and continuity equations. The governing equations are given in curvilinear coordinates ($\xi^i = \xi^i(x_1, x_2, x_3)$). Here, (ξ^1, ξ^2, ξ^3) is the tensor notation representation of the curvilinear coordinate (ξ, η, ζ), and (x_1, x_2, x_3) is the tensor notation representation of Cartesian coordinate (x, y, z), as shown in Fig. 2a. The governing equations in the curvilinear coordinate reads as follows in the tensor notation $(i, j, m, n = 1, 2, 3)$:

$$\begin{aligned}
&J\frac{\partial U^i}{\partial \xi^i} = 0, \\
&\frac{\partial U^i}{\partial t} = \xi^i_j\Big(\frac{\partial}{\partial \xi^n}(-U^n u_j) - \frac{\partial}{\partial \xi^n}(\frac{1}{\rho}\frac{\xi^n_j}{J}p) + \frac{\partial}{\partial \xi^n}((\nu+\nu_t)\frac{g^{nm}}{J}\frac{\partial u_j}{\partial \xi^m})\Big).
\end{aligned} \tag{4}$$

Here, ρ is the fluid density, ν is the kinematic viscosity, $J = |\partial(\xi^1, \xi^2, \xi^3)/\partial(x_1, x_2, x_3)|$ is the determinant of the Jacobian of the transformation $\xi^j_m = \partial \xi^j/\partial x_m$; g^{nm} is the contravariant metric of the transformation, $g^{nm} = \xi^n_j \xi^m_j$; p is the filtered pressure; $U^n = u_m \xi^n_m / J$ is the contravariant velocity of the fluid and ν_t is the subgrid-scale turbulent viscosity, which is modeled using the dynamic subgrid-scale model [44] as follows:

$$\nu_t = 2C_s\Delta^2(|s|)s_{ij}, \tag{5}$$

where $s_{ij} = 0.5(\frac{\partial u_i}{\partial x_j} + \frac{\partial u_j}{\partial x_i})$, $|s| = (\sqrt{2 s_{ij} s_{ij}}$. Here, a box filter with size of $\Delta = J^{-\frac{1}{3}}$, and C_s is the Smagorinsky coefficient computed dynamically [45] as follows

$$C_s = \frac{1}{2}\frac{< L_{ij}M_{ij} >}{< M_{ij}M_{ij} >}, \tag{6}$$

where

$$\begin{aligned}
L_{ij} &= -\widetilde{u_i u_j} + \widetilde{u}_i \widetilde{u}_j \\
M_{ij} &= \widetilde{\Delta}^2 \widetilde{s_{ij}}|\widetilde{s}| - \Delta^2 \widetilde{s_{ij}|s|},
\end{aligned} \tag{7}$$

where $(<>)$ denotes averaging along the homogeneous direction, which is the spanwise direction (z) in this study, and (~) represents the test filter which is twice of the grid filter ($\widetilde{\Delta} = 2\Delta$). Several studies have shown the suitability of dynamic subgrid-scale modeling for turbulent and transitional flows [46]. Our LES modeling is also validated extensively for fully developed turbulent [33] and transitional flows, e.g., flows over pitching airfoils, inclined plates [35], and circular cylinders [47].

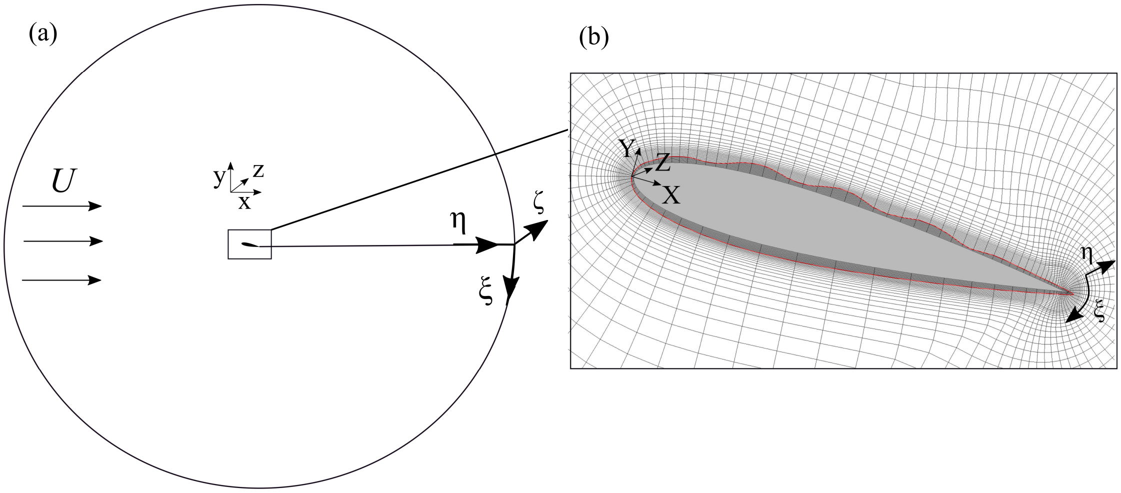

Fig. 2 The simulation set-up configuration, (a) flow and airfoil in the curvilinear and Cartesian coordinates, (b) representation of an undulating airfoil as an immersed boundary (red line) within the O-grid mesh. Every 10th point , and every 5th point in η and ξ directions are presented, respectively.

The moving boundaries are handled using the sharp-interface immersed boundary (IB) method described in detail in previous publications [48, 49]. In this method, the background grid is fixed and does not move with the boundaries, i.e., the airfoil surface (Fig. 2b) with the prescribed motion (Eqn. 1) is discretized by the triangular mesh and placed as a sharp-interface IB over the fixed background grid. The grid nodes inside the immersed boundary (solid nodes) are blanked out, while the velocity on the nodes that are exterior to, but adjacent to, the immersed boundary (IB nodes) are reconstructed using an interpolation along the normal to the boundary [50]. The background grid nodes are classified into solid, fluid and IB nodes by an efficient ray-tracing algorithm [49]. The classification of the grid nodes is performed once in the whole simulation for the static wall and once in each time step for the moving wall. The method is fully validated for flows with moving boundaries [49, 51, 52] and it has been used in various applications, including biological flows [53–57].

The Reynolds number, in the entire study, is chosen $Re = LU/\nu = 50,000$ based on the free flow velocity (U), airfoil chord length (L) and kinematic viscosity (ν). The fluid grid is an O-type grid (Fig. 2b) generated in the curvilinear frame (ξ, η, ζ), where η is normal to the airfoil surface, and ξ is parallel to the airfoil surface. This two dimensional domain is extruded in the $\zeta = z$ direction for $0.1L$ to generate a 3D domain. Note that, in regular body fitted grids $\eta = 0$ is attached to the surface of the airfoil, but here it is inside the immersed airfoil to capture the motion of the surface, i.e., $\eta = 0$ has a minimum normal distance of 0.012 from the surface of the airfoil (see the grids inside the immersed boundary in Fig. 2b). The boundary condition along ξ, ζ is periodic, and it is defined on $\eta(N_\eta)$ (outer boundary) as follows: It is inlet ($u_x = U$) in the upstream, (x<0), and it is Newman with a mass flux correction in the downstream (x>0). Note that the span size of the domain is chosen to be small to reduce computational costs. Therefore, the focus of this work is on spanwise-averaged results due to the limitation for capturing three-dimensional effects with this span size.

Table 1 The details of grid and time-step size of the simulation. R is the approximate radius of the O-type grid in Fig. 2a. N_ξ, N_η, and N_ζ are the number of points along ξ, η, and ζ directions, respectively. Δl_ξ^{min}, Δl_η^{min}, and Δl_ζ^{min} are the minimum grid spacing along ξ, η, and ζ directions, respectively.

grid	R	N_ξ	N_η	N_ζ	Δl_ξ^{min}	Δl_η^{min}	Δl_ζ^{min}
1	$15L$	421	281	21	$0.001L$	$0.0003L$	$0.005L$

The simulation set-up configuration, including the domain size and grid size are summarized in Table 1. The grid resolution is maintained $0.0003L$ along the η direction in the vicinity of the airfoil surface which is equivalent to a wall unit spacing of $\eta^+ = 0.9$, where $\eta^+ = \delta l_\eta u_\tau / \nu$, δl_η is the normal distance between the surface and first fluid node, and u_τ is the friction velocity. With this resolution, the viscous sublayer ($\eta^+ < 11.0$) of the boundary layer has at least 12 grid points along wall normal direction (η). The grid spacing remains constant up to $\eta = 0.022$, then it increases with a hyperbolic function to the boundaries. Using the curvilinear O-type grid in conjunction with the immersed boundary is suitable for low amplitude morphing simulations since it can capture the low amplitude oscillations with a lower computational cost compared to a Cartesian mesh. The time step is $0.0005L/U$ for the unactuated case and it ranges from $0.00032L/U$ to $0.00048L/U$ for the actuated cases, which corresponds to Courant-Friedrichs-Lewy numbers (CFL=$U\delta t/\Delta x$) less than 0.5.

The case studies are presented in Table 2. The first case is an unactuated airfoil and the wavelength of the actuated cases is $\lambda^* = 0.2$. Cases 2 to 4 are backward traveling wave actuated airfoils with constant amplitude and different reduced frequency (f^*) ranging from $f^* = 2.0$ to $f^* = 8$, i.e., corresponding to wave speeds $C^* = 0.4$ to $C^* = 1.6$. Case 5 is a high amplitude traveling wave actuation ($a^* = 0.008$, $f^* = 4.0$, and $C^* = 0.8$), case 6 is the forward traveling wave actuation ($a^* = 0.002$, $f^* = 4.0$, and $C^* = -0.8$), and case 7 is a standing wave actuation ($a^* = 0.002$, $f^* = 4.0$). Note

Table 2 The case studies, including unactuated airfoil, standing wave, forward traveling wave and backward traveling wave actuation with various frequencies and amplitudes. $\overline{C_L}$, $\overline{C_D}$, and $\overline{C_{Po}}$ are nondimensional, lift, drag and power coefficients, respectively. The wavelength is $\lambda^* = 0.2$ for all cases.

case	actuation type	f^*	a^*	C^*	$\overline{C_L}$	$\overline{C_D}$	$\overline{C_L}/\overline{C_D}$	$\overline{C_{Po}}$
1	unactuated	–	–	-	0.676	0.279	2.42	0.0
2	backward traveling wave	2.0	0.002	0.4	0.730	0.221	3.53	0.00012
3	backward traveling wave	4.0	0.002	0.8	0.886	0.096	9.23	0.00017
4	backward traveling wave	8.0	0.002	1.6	0.935	0.088	10.62	0.00027
5	backward traveling wave	4.0	0.008	0.8	0.824	0.125	6.59	0.00035
6	forward traveling wave	4.0	0.002	-0.8	0.807	0.276	2.92	0.00019
7	standing wave	4.0	0.002	-	0.817	0.206	3.96	0.00017

that the positive and negative signs of the wave speeds correspond to forward and backward traveling waves, respectively.

III. Results

The mean lift, drag, lift to drag, and power coefficients for all cases are presented in Table 2. Lift coefficient is $\overline{C_L} = \overline{F_L}/(0.5\rho U^2 L)$, where $\overline{F_L}$ is the mean dimensional per unit of the span of the airfoil force acting on the airfoil along the y direction, and the mean drag coefficient is $\overline{C_D} = \overline{F_D}/(0.5\rho U^2 L)$, where $\overline{F_D}$ is the mean dimensional per unit of the span of the airfoil force acting on the airfoil along the x direction. The power coefficient is the mean power required to accelerate the fluid near the oscillating surface which is calculated as follows:

$$\overline{C_{Po}} = \frac{1}{(0.5\rho U^3)AT} \int_T \left(\int_A -p n_Y \dot{h} dA \right) dt. \tag{8}$$

where $\dot{h}$ is the time derivative of the lateral displacement (Y direction), i.e., the velocity of the surface oscillation, n_Y is the Y component of the surface normal, p is the fluid pressure on the oscillating surface, dA is the area of the surface element, A is the actuated area of the airfoil's suction side, and T is the integration time which is equivalent to about 80 cycles for the actuated cases and 35 nondimensional time (L/U) for the unactuated case.

The mean lift coefficients ($\overline{C_L}$) and drag coefficient ($\overline{C_D}$) are presented in Table 2, which shows that the lift coefficient increases and the drag coefficient decreases by any actuation. The lowest lift increase (7.4%) is for case 2 which has the lowest f^*, and the highest lift enhancement (38.3%) is for case 4, which has a high frequency backward traveling wave. Comparing the lift and drag coefficients of cases 2 to 4, which have a constant amplitude with different frequencies, indicates that the lift coefficient increases and the drag coefficient decreases by increasing the frequency, e.g., C_L has

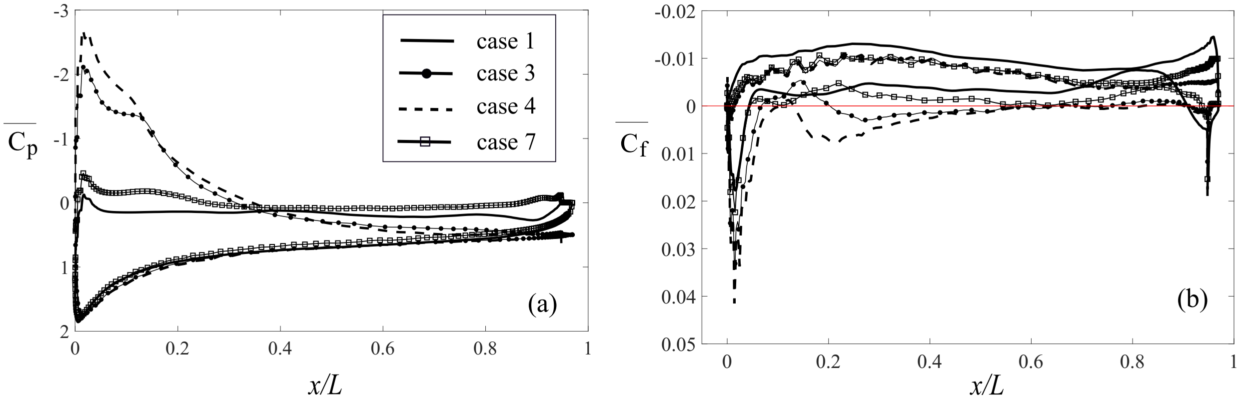

Fig. 3 The (a) mean spanwise-averaged pressure and (b) skin friction coefficients of the unactuated airfoil (case 1), the morphing airfoil with backward traveling wave actuations of $\mathbf{f}^* = 4.0$, $\mathbf{a}^* = 0.002$ (case 3) and $\mathbf{f}^* = 8.0$, $\mathbf{a}^* = 0.002$ (case 4), and a standing wave actuation $\mathbf{f}^* = 4.0$, $\mathbf{a}^* = 0.002$ (case 7).

increased by 16.4%, 31.0%, and 38.3% compared to the unactuated airfoil and C_D has decreased by 20.7%, 65.5%, and 68.4% compared to the unactuated airfoil, in cases 2, 3, and 4, respectively. By increasing the amplitude from 0.002, in case 3, to 0.008, in case 5, the lift coefficient has decreased and the drag coefficient has increased compared to the lower amplitude case, i.e., C_L has increased by 21.4% and C_D has decreased by 55.2% compared to the unactuated airfoil. Table 2 shows that the backward traveling wave actuation is more effective than either a forward traveling wave or a standing wave actuation in terms of improving the aerodynamic performance. The lift coefficient of case 3 is higher than cases 6 (forward traveling wave) and 7 (standing wave). The lift coefficient of cases 3, 6 and 7 has increased 31.0%, 19.3% and 20.4% compared to the unactuated case, respectively. In addition, C_D of these cases have reduced by 65.5%, 1.1%, and 26.1%, respectively, compared to the unactuated airfoil. Among these cases, case 4 has the highest lift to drag ratio, e.g., $\overline{C_L}/\overline{C_D} = 10.62$ which is about 4 times greater than the unactuated case (Table 2). In addition, among the cases with the same frequency but different actuation type, i.e., cases 3, 5, 6 and 7, the low amplitude traveling wave actuation (case 3) has the highest $\overline{C_L}/\overline{C_D}$ of 9.23 and the forward traveling wave actuation (case 6) has the lowest one, i.e., it is only 20.6% higher than the unactuated case. In fact, based on the aerodynamic performance observed in Table 2, the low-amplitude traveling wave actuations are more effective than either forward traveling wave or standing wave actuations. The required power for these oscillations is small compared to the drag power loss ($U \times C_D$). For instance, the C_{Po} is less than 0.0004 for all cases while the drag loss power is O(0.1).

The enhancement of lift coefficient by the actuations in Table 2 can better be observed by the distribution of the mean pressure coefficient around the circumference of the airfoil. The pressure coefficient can be expressed as

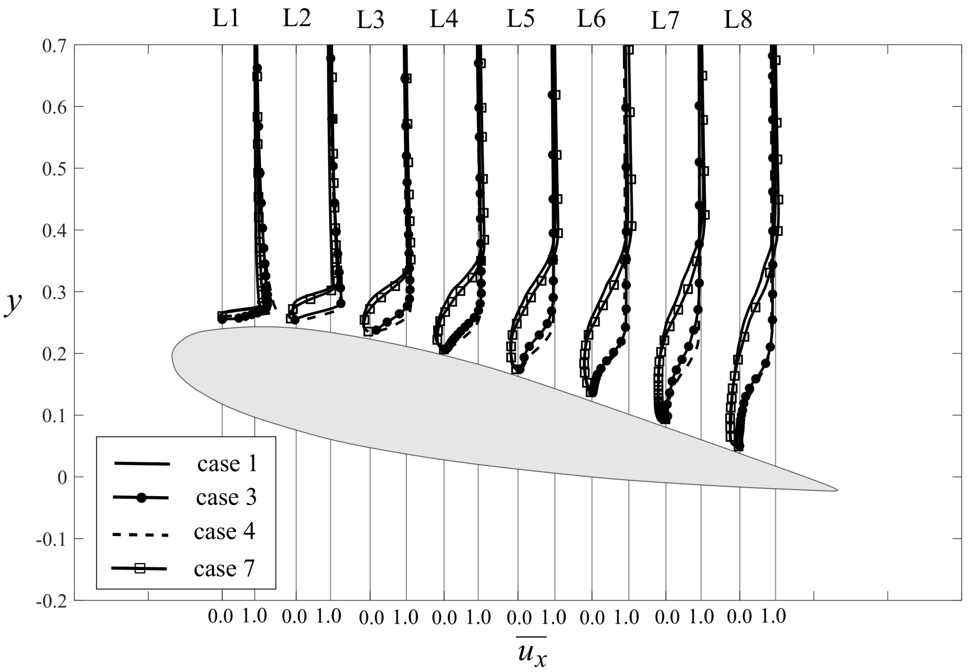

Fig. 4 The profile of the mean spanwise-averaged streamwise velocity ($\overline{u_x}$) for cases 1, 3, 4, and 7 at 8 different sections spaced by 0.1L, starting from L1 at 0.1L to L8 at 0.8L of the airfoil's leading edges.

$C_p = 2p/(\rho U^2)$, where the reference pressure (zero pressure) is pressure at leading edge ($X, Y = 0$). The mean pressure coefficient ($\overline{C_p}$) is computed by averaging the pressure of the grid point adjacent to the surface. The mean pressure coefficient is plotted for cases 1, 3, 4, and 7 in Fig. 3a. The profile of $\overline{C_p}$ (Fig. 3a) shows that the lift coefficient of the actuated airfoil increases because $\overline{C_p}$ of the suction side of the airfoil decreases in the vicinity of the leading edge, i.e., the negative C_p contributes to lift. The profile of the pressure coefficient of the unactuated case shows the stall condition. For instance, on the suction side of the unactuated airfoil, the $\overline{C_p}$ decreases from the leading edge, i.e., it has a peak at $x = 0.03$, then it has a flat-like profile at $0.05 < x < 0.83$, and finally, it decreases again near the trailing edge, similar to the $\overline{C_p}$ profile reported by Puri et al. [23]. When a backward traveling wave actuation (cases 3 and 4) is applied, the peak of $\overline{C_p}$ increases substantially (pressure decreases) compared to the unactuated airfoil, i.e., lift coefficient increases. In case 4, there is a pressure recovery from the peak ($x = 0.03$) up to the trailing edge. However, for cases 3, there is a plateau from $x = 0.10$ to $x = 0.18$, and then the pressure recovery occurs toward the trailing edge. When a standing wave actuation (case 7) is applied, the peak is higher than the unactuated airfoil but it is lower than the one generated by the traveling wave actuations (cases 3 and 4).

Flow over an airfoil at the stall angle of attack becomes separated from the leading edge [58]. By using a flow control technique, the flow separation might decrease either by delaying the separation to further backward or reattaching the separated flow further backward. The flow separation and reattachment is an unsteady process and, consequently, the separation/reattachment location varies with time. Here, to quantify the effect of actuations on the flow separation, the separation/reattachment is defined based on the mean skin friction ($\overline{C_f}$). The mean skin friction is the mean spanwise-averaged of instantaneous skin friction on the points adjacent to the surface, where the instantaneous skin friction is $C_f = 2/Re(\partial u_x^*/\partial y^*)$ and the velocity gradient in the curvilinear coordinates is $\partial u_x^*/\partial y^* = (\partial u_x^*/\partial \xi)(\partial \xi/\partial y^*) + (\partial u_x^*/\partial \eta)(\partial \eta/\partial y^*))$. Based on the mean skin friction, the separation and reattachment location on the suction side are defined as the points where the mean skin friction ($\overline{C_f}$) becomes negative and positive, respectively. The distribution of $\overline{C_f}$ indicates a high positive value on the suction side near the trailing edge, e.g., $x > 0.9L$. However, this positive value does not account for a flow reattachment. In fact, the positive C_f at those locations e.g., $x/L > 0.9$ is due to a strong trailing edge vortex which is present in the mean flow similar to the instantaneous ones (Fig. 5a). The C_f plot indicates that the traveling wave actuations moves the separation point further backward toward the trailing edge. Based on Fig. 3b, the flow of the unactuated airfoil becomes separated from $x = 0.05L$ without reattachment. The skin friction of case 7 is similar to case 1, i.e., flow separates from the leading edge without reattachment. In case 3, flow separates at $x = 0.1L$, and reattaches at $x = 0.18L$, where the plateau region for pressure coefficient is created (Fig. 3a). Afterwards, flow becomes separated at $x = 0.78L$. Nevertheless, in case 4, flow remains attached from the leading edge up to $x = 0.75L$. The flow attachment for cases 3 and 4 results in a lower pressure coefficient at those sections as it was shown in Fig. 3a.

In addition to the location of the separation point, the profile of the mean streamwise velocity can demonstrate effects of the actuations on flow separation by quantifying the reverse flow on the suction side. The profile of the mean spanwise-averaged streamwise velocity ($\overline{u_x}$) for the unactuated airfoil and actuated cases 3, 4, and 7 are presented in Fig. 4. As it can be observed in Fig. 4, there is a strong reverse flow at section L2 to L6 for the unactuated and standing wave cases, whereas there is no reverse flow at that locations for the traveling cases (cases 3 and 4). Note that the standing wave actuation does not suppress the flow separation similar to the traveling wave one, but it reduces the reverse flow relative to the unactuated case. Flow becomes separated for cases 3 and 4 near the trailing edge (section L8) while the reverse flow is less than the unactuated and standing wave cases, as it was also observed in Fig. 3b.

To visualize the instantaneous flow separation and attachment more clearly, the spanwise-averaged instantaneous

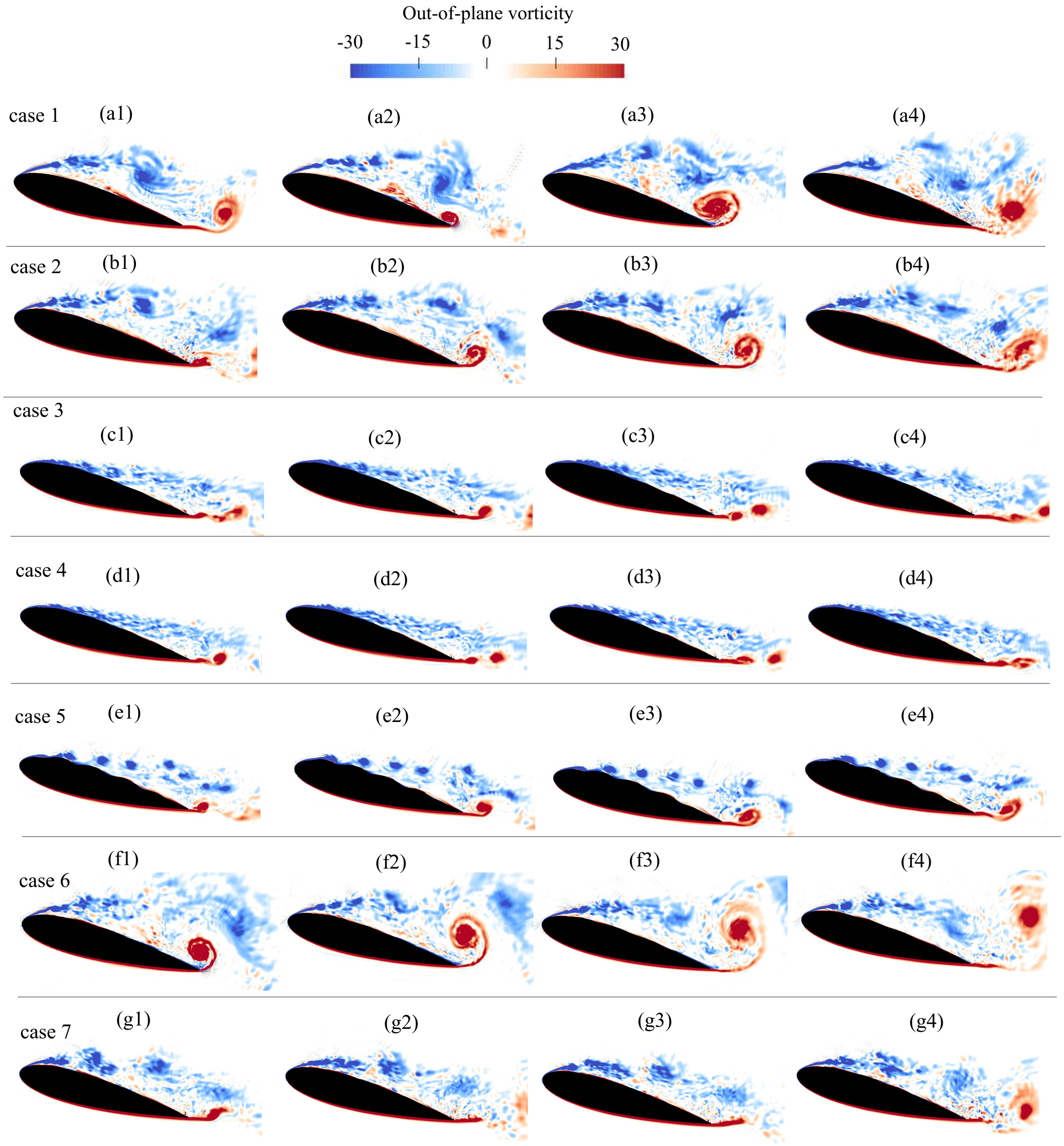

Fig. 5 Instantaneous flow field visualized by the contours of out-of-plane vorticity (ω_z).

out-of-plane vorticity of the seven cases (Table 2) at four different time instants are presented in Fig. 5. Flow is fully separated over the suction side of the unactuated airfoil, i.e., the shear layer separates from the leading edge and sheds to the wake, and on the trailing edge an unstable counter clockwise vortex (trailing edge vortex) is generated (Fig. 5a3). Both the shear layer and trailing edge separation decrease when any type of actuation is applied. Similar to the mean flow (Fig. 4), the separation reduction is more significant when a traveling wave actuation with $f^* \geq 4$ (cases 3 and 4) is applied, i.e., the shear layer is closer to the airfoil's surface near the leading edge.

When the low frequency traveling actuation (case 2) is applied, the flow separates from the leading edge. Nevertheless, the separated shear layer is closer to the airfoil surface, and the trailing edge vortex is smaller compared to the unactuated airfoil (compare Fig. 5b3 and Fig. 5a3). By increasing the frequency to 4 and 8, the shear layer separation decreases (Fig. 5c1 to c4 and Fig. 5d1 to d4), and size of the trailing edge vortex decreases due to delayed separation. By increasing the amplitude to 0.008 in case 5, the shear layer becomes unstable near the actuation point ($x > 0.1$). The higher amplitude traveling wave oscillations generates large coherent structures that become separated from the airfoil surface and shed periodically with the oscillations frequency into the wake. Nevertheless, the traveling wave oscillations increase the axial momentum and reduce the flow separation near the trailing edge. The generation of the coherent structures by the traveling waves have also been reported in the previous studies [34, 35]. The forward traveling wave actuation (case 6), in contrast to the backward traveling wave one does not reduce flow separation (Fig. 5f). In case 6, the shear layer is fully separated while a large trailing edge vortex is generated at the trailing edge, similar to the unactuated case (Fig 5a). The standing wave actuation brings the shear layer closer to the airfoil surface (Fig. 5g) but not as closer as the traveling wave one (Fig. 5c).

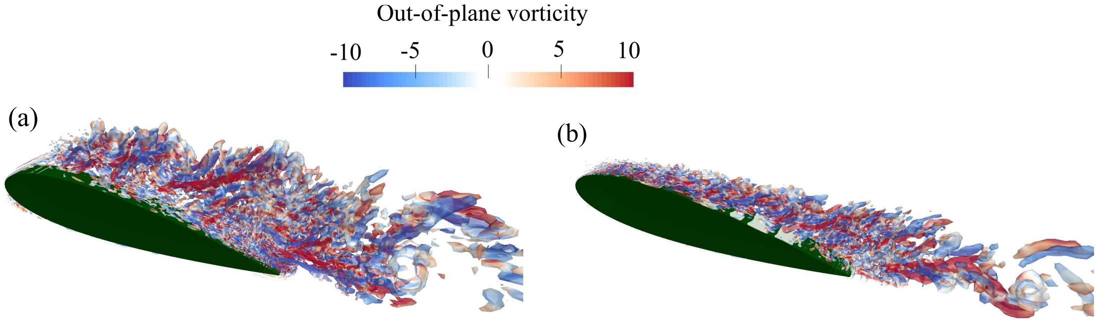

Fig. 6 Three dimensional vortical structures visualized by the instantaneous isosurfaces of the Q-Criterion (Q=20) colored by the out-of-plane vorticity for (a) case 1 (unactuated airfoil) and, (b) case 4 (traveling wave morphing airfoil with $\mathbf{f}^* = 8.0, \mathbf{a}^* = 0.002$).

Figure 6 presents the three dimensional turbulent flow structure (vortices) visualized using iso-surface of Q-criterion that colored by out-of-plane vorticity for unactuated airfoil (case 1) and morphing airfoil with $f^* = 8.0, a^* = 0.002$ (case 4). By comparing Fig. 6a and Fig. 6b, it can be observed that the low amplitude traveling wave morphing reduces the flow separation, similar to the observation of 2D flow field in Fig. 5.

IV. Discussion and Conclusion

Previous studies [33, 59, 60] have shown that backward traveling waves can increase the streamwise fluid momentum and decrease the drag force, which theoretically scales with $(a^* f^*)^2(1 - 1/C^{*2})$ [35, 60]. Recently, Akbarzadeh and Borazjani [35] observed that traveling wave oscillations with significantly higher amplitudes ($a^* = 0.01$) and frequency ($f^* = 20$) but the same wavelength ($\lambda^* = 0.2$) as of this study on an inclined plate could reduce the flow separation and drag coefficient but they could not postpone the stall and reattach the flow to the leading edge because of the plate's sharp leading edge. However, in this study, it was shown that a surface morphing in the form of backward traveling waves can suppress the static stall and delay separation. The results of our LES show that a low amplitude traveling wave ($a = 0.002L$) with reduced frequencies 4.0 and 8.0, and $\lambda^* = 0.2$ can suppress the stall and increases the lift coefficient by about 34%. The lift enhancement is high compared to our previous study for this airfoil at $AOA = 10^o$ in which the lift increased only by about 4% [59] because flow control is, typically, more effective at stall and post stall angles where the flow is massively separated [7].

The flow visualizations (Figs. 4 and 5) indicate that the backward traveling wave actuations are more effective than other actuations because they accelerate the fluid adjacent to the surface along the streamwise direction [35], i.e., increase the momentum of the fluid near the surface directly, similar to a swimming fish [60]. While the backward traveling waves with frequency greater than 4, e.g., cases 3 and 4, suppress the stall, a lower frequency of $f^* = 2$ (case 2) does not influence the flow separation significantly. Based on the results of cases 2, 3 and 4, it can be concluded that the frequency needs to be high enough to control the flow separation because, theoretically, the axial force created by traveling waves scales with $((af)^2(1 - 1/(\lambda f)^2))$ [35, 60]. However, by increasing the wave amplitude in case 6, the shear layer is only attached up to the actuation point and it becomes unstable after that point. Afterwards, the unstable shear layer sheds into the wake in the form of large periodic coherent structures. Therefore, the flow separation has increased in case 6 compared to case 3, although the amplitude has increased. The reason for the shear layer destabilization in case 6 is, probably, the high wave steepness (a/λ) as the shear layer separates from the first trough of the traveling wave (Fig. 5e). In fact, a steep surface deformation can destabilize an attached shear layer and enhance the separation [33, 61]. In contrast to the backward traveling waves, the forward traveling wave actuation is the least effective actuation because it increases the reverse flow near the wavy surface [32, 33]. Finally, the standing wave actuation (case 7) reduced the flow separation though it does not increase the boundary layer's streamwise momentum directly. Standing waves reduce the flow separation by triggering the Kelvin-Helmholtz instability [13] and enhancing the mixing of the separated shear layer with the low momentum flow of near the surface similar to periodic excitation flow control mechanism [7]. Note that this mixing occurs for other actuations, including backward and forward traveling waves, because the airfoil surface oscillates. The oscillating surface induces a normal velocity that scales with $0.05U < u_Y = O(2\pi f a) < 0.1U$ which is close the velocity induced by the surface in previous studies [13]. In fact, in traveling wave actuation cases, both (i) the axial momentum induced to the flow and (ii) the triggering of instabilities affect the flow separation. Nevertheless, understanding the effect of each of these two terms, i.e., axial momentum induced to the flow versus triggering the instabilities, on the flow separation, or investigating the effects of wavelength at the stall and post stall angles of attack can be an interesting topic for future studies.

Acknowledgments

This work was partly supported by the National Science Foundation (NSF) grants CBET 1453982 and 1905355. The computational resources were partly provided by the High Performance Research Computing (HPRC) facilities at Texas A&M University.

References

[1] Mueller, T. J., and DeLaurier, J. D., "Aerodynamics of small vehicles," *Annual review of fluid mechanics*, Vol. 35, No. 1, 2003, pp. 89–111. doi:10.1146/annurev.fluid.35.101101.161102.

[2] Shyy, W., Lian, Y., Tang, J., Viieru, D., and Liu, H., *Aerodynamics of low Reynolds number flyers*, Vol. 22, Cambridge University Press, 2007. doi:https://doi.org/10.1017/CBO9780511551154.

[3] Postl, D., Balzer, W., and Fasel, H. F., "Control of laminar separation using pulsed vortex generator jets: direct numerical simulations," *Journal of Fluid Mechanics*, Vol. 676, 2011, pp. 81–109. doi:10.1017/jfm.2011.34.

[4] Chang, P. K., "Chapter XII - Control of Separation of Flow," *Separation of Flow*, Pergamon, 1970, pp. 716 – 752. doi: https://doi.org/10.1016/B978-0-08-013441-3.50016-2.

[5] Aubrun, S., McNally, J., Alvi, F., and Kourta, A., "Separation flow control on a generic ground vehicle using steady microjet arrays," *Experiments in Fluids*, Vol. 51, No. 5, 2011, pp. 1177–1187. doi:10.1007/s00348-011-1132-0.

[6] Donovan, J., Kral, L., and Cary, A., "Active flow control applied to an airfoil," *36th AIAA Aerospace Sciences Meeting and Exhibit*, American Institute of Aeronautics and Astronautics, 1998. doi:10.2514/6.1998-210.

[7] Greenblatt, D., and Wygnanski, I. J., “The control of flow separation by periodic excitation,” *Progress in aerospace Sciences*, Vol. 36, No. 7, 2000, pp. 487–545. doi:https://doi.org/10.1016/S0376-0421(00)00008-7.

[8] Seifert, A., Darabi, A., and Wyganski, I., “Delay of airfoil stall by periodic excitation,” *Journal of Aircraft*, Vol. 33, No. 4, 1996, pp. 691–698. doi:10.2514/3.47003.

[9] Wu, J.-Z., Lu, X.-Y., Denny, A. G., Fan, M., and Wu, J.-M., “Post-stall flow control on an airfoil by local unsteady forcing,” *Journal of Fluid Mechanics*, Vol. 371, 1998, pp. 21–58. doi:10.1017/s0022112098002055.

[10] Glezer, A., and Amitay, M., “Synthetic jets,” *Annual review of fluid mechanics*, Vol. 34, No. 1, 2002, pp. 503–529. doi:https://doi.org/10.1146/annurev.fluid.34.090501.094913.

[11] Amitay, M., Smith, D. R., Kibens, V., Parekh, D. E., and Glezer, A., “Aerodynamic Flow Control over an Unconventional Airfoil Using Synthetic Jet Actuators,” *AIAA Journal*, Vol. 39, No. 3, 2001, pp. 361–370. doi:10.2514/2.1323.

[12] Buchmann, N. A., Atkinson, C., and Soria, J., “Influence of ZNMF jet flow control on the spatio-temporal flow structure over a NACA-0015 airfoil,” *Experiments in Fluids*, Vol. 54, No. 3, 2013. doi:10.1007/s00348-013-1485-7.

[13] Jones, G., Santer, M., Debiasi, M., and Papadakis, G., “Control of flow separation around an airfoil at low Reynolds numbers using periodic surface morphing,” *Journal of Fluids and Structures*, Vol. 76, 2018, pp. 536–557. doi:https://doi.org/10.1016/j.jfluidstructs.2017.11.008.

[14] Park, Y. W., Lee, S.-G., Lee, D.-H., and Hong, S., “Stall Control with Local Surface Buzzing on a NACA 0012 Airfoil,” *AIAA Journal*, Vol. 39, No. 7, 2001, pp. 1400–1402. doi:10.2514/2.1460.

[15] Jodin, G., Motta, V., Scheller, J., Duhayon, E., Döll, C., Rouchon, J., and Braza, M., “Dynamics of a hybrid morphing wing with active open loop vibrating trailing edge by time-resolved PIV and force measures,” *Journal of Fluids and Structures*, Vol. 74, 2017, pp. 263–290. doi:10.1016/j.jfluidstructs.2017.06.015.

[16] Katz, Y., Nishri, B., and Wygnanski, I., “The delay of turbulent boundary layer separation by oscillatory active control,” *Physics of Fluids A: Fluid Dynamics*, Vol. 1, No. 2, 1989, pp. 179–181. doi:10.1063/1.857555.

[17] Lyu, Z., and Martins, J. R. R. A., “Aerodynamic Shape Optimization of an Adaptive Morphing Trailing-Edge Wing,” *Journal of Aircraft*, Vol. 52, No. 6, 2015, pp. 1951–1970. doi:10.2514/1.c033116.

[18] Seifert, A., Eliahu, S., Greenblatt, D., and Wygnanski, I., “Use of Piezoelectric Actuators for Airfoil Separation Control,” *AIAA Journal*, Vol. 36, No. 8, 1998, pp. 1535–1537. doi:10.2514/2.549.

[19] Cattafesta, L. N., and Sheplak, M., "Actuators for Active Flow Control," *Annual Review of Fluid Mechanics*, Vol. 43, No. 1, 2011, pp. 247–272. doi:10.1146/annurev-fluid-122109-160634.

[20] Jones, G., Santer, M., and Papadakis, G., "Control of low Reynolds number flow around an airfoil using periodic surface morphing: A numerical study," *Journal of Fluids and Structures*, Vol. 76, 2018, pp. 95–115. doi:10.1016/j.jfluidstructs.2017.09.009.

[21] Kang, W., Lei, P., Zhang, J., and Xu, M., "Effects of local oscillation of airfoil surface on lift enhancement at low Reynolds number," *Journal of Fluids and Structures*, Vol. 57, 2015, pp. 49–65. doi:10.1016/j.jfluidstructs.2015.05.009.

[22] You, D., Wang, M., and Moin, P., "Large-Eddy Simulation of Flow over a Wall-Mounted Hump with Separation Control," *AIAA Journal*, Vol. 44, No. 11, 2006, pp. 2571–2577. doi:10.2514/1.21989.

[23] Puri, K., Laufer, M., Müller-Vahl, H., Greenblatt, D., and Frankel, S. H., "Computations of Active Flow Control Via Steady Blowing Over a NACA-0018 Airfoil: Implicit LES and RANS Validated Against Experimental Data," *2018 AIAA Aerospace Sciences Meeting*, American Institute of Aeronautics and Astronautics, 2018. doi:10.2514/6.2018-0792.

[24] Rizzetta, D. P., Visbal, M. R., and Morgan, P. E., "A high-order compact finite-difference scheme for large-eddy simulation of active flow control," *Progress in Aerospace Sciences*, Vol. 44, No. 6, 2008, pp. 397–426. doi:https://doi.org/10.1016/j.paerosci.2008.06.003.

[25] Krzysiak, A., and Narkiewicz, J., "Aerodynamic Loads on Airfoil with Trailing-Edge Flap Pitching with Different Frequencies," *Journal of Aircraft*, Vol. 43, No. 2, 2006, pp. 407–418. doi:10.2514/1.15597.

[26] Abdessemed, C., Yao, Y., Bouferrouk, A., and Narayan, P., "Aerodynamic Analysis of a harmonically Morphing Flap Using a Hybrid Turbulence Model and Dynamic Meshing," *2018 Applied Aerodynamics Conference*, American Institute of Aeronautics and Astronautics, 2018. doi:10.2514/6.2018-3813.

[27] Lee, T., and Gerontakos, P., "Unsteady Airfoil with Dynamic Leading- and Trailing-Edge Flaps," *Journal of Aircraft*, Vol. 46, No. 3, 2009, pp. 1076–1081. doi:10.2514/1.42431.

[28] Munday, D., and Jacob, J., "Active Control of Separation on a Wing with Oscillating Camber," *Journal of Aircraft*, Vol. 39, No. 1, 2002, pp. 187–189. doi:10.2514/2.2915.

[29] Di, G., Wu, Z., and Huang, D., "The research on active flow control method with vibration diaphragm on a NACA0012 airfoil at different stalled angles of attack," *Aerospace Science and Technology*, Vol. 69, 2017, pp. 76–86. doi:10.1016/j.ast.2017.06.020.

[30] Ashill, P. R., Fulker, J. L., and Hackett, K. C., "A review of recent developments in flow control," *The Aeronautical Journal*, Vol. 109, No. 1095, 2005, pp. 205–232. doi:10.1017/s0001924000005200.

[31] Munday, D., Jacob, J., Hauser, T., and Huang, G., "Experimental and Numerical Investigation ofAerodynamic Flow Control Using Oscillating Adaptive Surfaces," *1st Flow Control Conference*, American Institute of Aeronautics and Astronautics, 2002. doi:10.2514/6.2002-2837.

[32] Shen, L., Zhang, X., Yue, D. K. P., and Triantafyllou, M. S., "Turbulent flow over a flexible wall undergoing a streamwise travelling wave motion," *Journal of Fluid Mechanics*, Vol. 484, 2003, pp. 197–221. doi:10.1017/s0022112003004294.

[33] Akbarzadeh, A. M., and Borazjani, I., "Large eddy simulations of a turbulent channel flow with a deforming wall undergoing high steepness traveling waves," *Physics of Fluids*, Vol. 31, No. 12, 2019, p. 125107. doi:10.1063/1.5131268.

[34] Wu, C.-J., Wang, L., and Wu, J.-Z., "Suppression of the von Kármán vortex street behind a circular cylinder by a travelling wave generated by a flexible surface," *Journal of Fluid Mechanics*, Vol. 574, 2007, p. 365–391. doi:10.1017/S0022112006004150.

[35] Akbarzadeh, A. M., and Borazjani, I., "Reducing flow separation of an inclined plate via travelling waves," *Journal of Fluid Mechanics*, Vol. 880, 2019, pp. 831–863. doi:10.1017/jfm.2019.705.

[36] Taneda, S., "Visual study of unsteady separated flows around bodies," *Progress in Aerospace Sciences*, Vol. 17, 1976, pp. 287–348. doi:https://doi.org/10.1016/0376-0421(76)90011-7.

[37] Borazjani, I., and Sotiropoulos, F., "Numerical investigation of the hydrodynamics of carangiform swimming in the transitional and inertial flow regimes," *Journal of Experimental Biology*, Vol. 211, 2008, pp. 1541–1558. doi:doi:10.1242/jeb.015644.

[38] Akbarzadeh, A., and Borazjani, I., "A numerical study on controlling flow separation via surface morphing in the form of backward traveling waves," *AIAA Aviation 2019 Forum*, 2019, p. 3589. doi:https://doi.org/10.2514/6.2019-3589.

[39] Barbarino, S., Bilgen, O., Ajaj, R. M., Friswell, M. I., and Inman, D. J., "A Review of Morphing Aircraft," *Journal of Intelligent Material Systems and Structures*, Vol. 22, No. 9, 2011, pp. 823–877. doi:10.1177/1045389x11414084.

[40] Lee, A. J., Moosavian, A., and Inman, D. J., "A piezoelectrically generated bistable laminate for morphing," *Materials Letters*, Vol. 190, 2017, pp. 123–126. doi:10.1016/j.matlet.2017.01.005.

[41] Bani-Hani, M., and Karami, M., "Analytical structural optimization and experimental verifications for traveling wave generation in self-assembling swimming smart boxes," *Smart Materials and Structures*, Vol. 24, No. 9, 2015, p. 094005. doi:https://doi.org/10.1088/0964-1726/24/9/094005.

[42] Müller-Vahl, H. F., Strangfeld, C., Nayeri, C. N., Paschereit, C. O., and Greenblatt, D., "Control of Thick Airfoil, Deep Dynamic Stall Using Steady Blowing," *AIAA Journal*, Vol. 53, No. 2, 2015, pp. 277–295. doi:10.2514/1.j053090.

[43] Gerakopulos, R., Boutilier, M., and Yarusevych, S., "Aerodynamic Characterization of a NACA 0018 Airfoil at Low Reynolds Numbers," *40th Fluid Dynamics Conference and Exhibit*, American Institute of Aeronautics and Astronautics, 2010. doi:10.2514/6.2010-4629.

[44] Germano, M., Piomelli, U., Moin, P., and Cabot, W. H., "A dynamic subgrid-scale eddy viscosity model," *Physics of Fluids A: Fluid Dynamics*, Vol. 3, No. 7, 1991, pp. 1760–1765. doi:https://doi.org/10.1063/1.857955.

[45] Lilly, D. K., "A proposed modification of the Germano subgrid-scale closure method," *Physics of Fluids A: Fluid Dynamics*, Vol. 4, No. 3, 1992, pp. 633–635. doi:10.1063/1.858280.

[46] Rizzetta, D., Visbal, M., and Blaisdell, G., "Application of a high-order compact difference scheme to large-eddy and direct numerical simulation," *30th Fluid Dynamics Conference*, 1999, p. 3714. doi:https://doi.org/10.2514/6.1999-3714.

[47] Bottom II, R., Borazjani, I., Blevins, E., and Lauder, G., "Hydrodynamics of swimming in stingrays: numerical simulations and the role of the leading-edge vortex," *Journal of Fluid Mechanics*, Vol. 788, 2016, pp. 407–443. doi:https://doi.org/10.1017/jfm.2015.702.

[48] Ge, L., and Sotiropoulos, F., "A numerical method for solving the 3D unsteady incompressible Navier–Stokes equations in curvilinear domains with complex immersed boundaries," *Journal of computational physics*, Vol. 225, No. 2, 2007, pp. 1782–1809. doi:10.1016/j.jcp.2007.02.017.

[49] Borazjani, I., Ge, L., and Sotiropoulos, F., "Curvilinear immersed boundary method for simulating fluid structure interaction with complex 3D rigid bodies," *Journal of Computational physics*, Vol. 227, No. 16, 2008, pp. 7587–7620. doi:https://doi.org/10.1016/j.jcp.2008.04.028.

[50] Gilmanov, A., and Sotiropoulos, F., "A hybrid Cartesian/immersed boundary method for simulating flows with 3D, geometrically complex, moving bodies," *Journal of Computational Physics*, Vol. 207, No. 2, 2005, pp. 457 – 492. doi:https://doi.org/10.1016/j.jcp.2005.01.020.

[51] Borazjani, I., Sotiropoulos, F., Tytell, E. D., and Lauder, G. V., "Hydrodynamics of the bluegill sunfish C-start escape response: three-dimensional simulations and comparison with experimental data," *Journal of Experimental Biology*, Vol. 215, No. 4, 2012, pp. 671–684. doi:10.1242/jeb.063016.

[52] Asgharzadeh, H., and Borazjani, I., "A Newton–Krylov method with an approximate analytical Jacobian for implicit solution of Navier–Stokes equations on staggered overset-curvilinear grids with immersed boundaries," *Journal of computational physics*, Vol. 331, 2017, pp. 227–256. doi:10.1016/j.jcp.2016.11.033.

[53] Asgharzadeh, H., Asadi, H., Meng, H., and Borazjani, I., "A non-dimensional parameter for classification of the flow in intracranial aneurysms. II. Patient-specific geometries," *Physics of Fluids*, Vol. 31, No. 3, 2019, p. 031905. doi:10.1063/1.5081451.

[54] Hedayat, M., and Borazjani, I., "Comparison of platelet activation through hinge vs bulk flow in bileaflet mechanical heart valves," *Journal of Biomechanics*, Vol. 83, 2019, pp. 280–290. doi:10.1016/j.jbiomech.2018.12.003.

[55] Asadi, H., Asgharzadeh, H., and Borazjani, I., "On the scaling of propagation of periodically generated vortex rings," *Journal of Fluid Mechanics*, Vol. 853, 2018, pp. 150–170. doi:10.1017/jfm.2018.529.

[56] Ogunka, U. E., Daghooghi, M., Akbarzadeh, A. M., and Borazjani, I., "The Ground Effect in Anguilliform Swimming," *Biomimetics*, Vol. 5, No. 1, 2020, p. 9. doi:https://doi.org/10.3390/biomimetics5010009.

[57] Borazjani, I., and Akbarzadeh, A., "Large Eddy Simulations of Flows with Moving Boundaries," *Modeling and Simulation of Turbulent Mixing and Reaction*, Springer Singapore, 2020, pp. 201–225. doi:10.1007/978-981-15-2643-5_9.

[58] Mittal, R., Kotapati, R., and Cattafesta, L., "Numerical study of resonant interactions and flow control in a canonical separated flow," *43rd AIAA Aerospace Sciences Meeting and Exhibit*, 2005, p. 1261. doi:0.2514/6.2005-1261.

[59] Akbarzadeh, A., and Iman, B., "Video: Controlling flow separation using traveling wave actuation," *72th Annual Meeting of the APS Division of Fluid Dynamics - Gallery of Fluid Motion*, American Physical Society, 2019. doi:10.1103/aps.dfd.2019.gfm.v0078.

[60] Lighthill, M. J., "Note on the swimming of slender fish," *Journal of Fluid Mechanics*, Vol. 9, No. 2, 1960, p. 305–317. doi:10.1017/S0022112060001110.

[61] Buckles, J., Hanratty, T. J., and Adrian, R. J., "Turbulent flow over large-amplitude wavy surfaces," *Journal of Fluid Mechanics*, Vol. 140, No. -1, 1984, p. 27. doi:10.1017/s0022112084000495.